LAUNCH, RENDEZVOUS AND DOCKING ANALYSIS FOR A MODULAR SELF ASSEMBLING SPACE TELESCOPE

Erik Gustafson
Masters of Engineering Report
Cornell University
Sibley School of Mechanical and Aerospace Engineering

May 20, 2019

Abstract

Creating large space telescopes has been a topic of interest for many years, as increasing our observational capabilities are key to answering a variety of astrophysical and planetary science questions. One approach is to construct a telescope out of modules that assemble themselves into a primary mirror surface. Some of the key challenges to this approach are ensuring there is sufficient launch capability to deploy the modules, and that they are capable of rendezvousing and docking. This report predicts the United State's future launch capacity, analyzes ability of modules to rendezvous about the Earth-Sun L2 point with solar sails, and investigates collision mechanics between two solar sails, and finds solutions to all of these problems that are sufficient to support the concept of operations proposed and investigated by Dr. Dmitry Savransky and his team for the NASA Innovative Advanced Concepts program.

1 Introduction

Dr. Dmitry Savransky proposed a mission concept in 2018 that called for a modular, self-assembling 30+ m diameter reflective space telescope [1]. The concept of operations calls for 840 1m diameter hexagonal units, with each unit topped with an active mirror assembly. Modules will be launched as payloads of opportunity, and will navigate to the Earth-Sun L2 point with deployable solar sails, where they will enter into a quasi-periodic Lissajous parking orbit. When modules come within 1000 km of each other, they will use their solar sails to rendezvous, and then they will dock.

When modules dock, they will initially collide, with the booms of their solar sails making contact first. The the vibration in the booms will dissipate the energy of the collision, and bring both modules to the same velocity. The docking scheme is outlined in Figure 1

Launches will occur over 7 years, with the telescope being assembled within 10 years of the first launch.

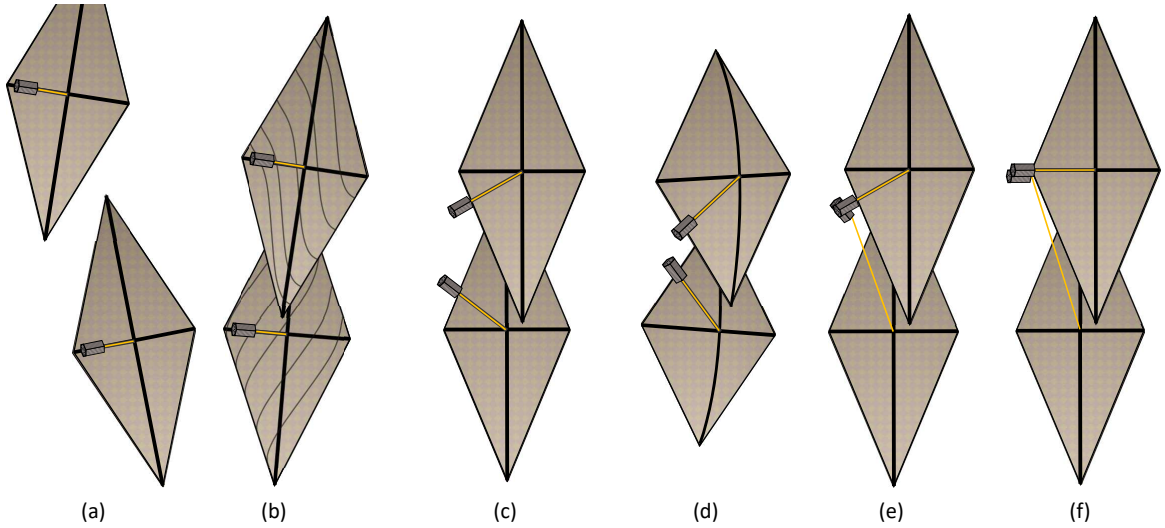

Figure 1: Schematic of module docking. (a) A module places itself on an intercept trajectory with another module or sub-assembly. (b) The sails make contact and stick via embedded hook-and-loop material or hooks on the booms. Energy is dissipated via sail vibration. (c-d) The sails reef their facing sides and the spacecraft pivot (using module ACS/RCS) on their extended tethers. (e) Controllable electromagnets on the modules' sides force them into the proper orientation and alignment. (f) Mechanical interconnects link the modules, the sails unfurl and one tether is optionally released (based on the size of the sub-assembly).

3 aspects of this concept of operations were investigated to establish feasibility; 1) the ability of launches from the United States to carry 840 modules as payloads of opportunity within the mission timeline. 2) the ability of modules to rendezvous on the Lissajous orbit using their solar sails as the sole means of propulsion. 3) the collision mechanics of solar sails colliding, and the docking procedures required to assemble the primary mirror.

2 Historical Launch Analysis

Predicting future launch capability is central to determining how many segments can be launched as payloads of opportunity, and how many would have to be launched on rockets dedicated to this mission. To predict future launch capability, a historical launch analysis was performed, which was targeted at recent launches (2016-2018) from the United States.

This process began by gathering data on launch and payload history. Launch data was collected from the Orbital Launch Log [2], last updated in May of 2018. It includes data on launch dates, sites, vehicles, and the Committee on Space Research (COSPAR) designation for each payload on the launch.

Payload data was collected from the Union of Concerned Scientists' satellite catalogue [3], which contains orbital elements and payload mass for most satellites in order. Satellites were matched to launches using COSPAR designations.

Launches were selected based on their launch site, and year. For this analysis, launches from Kennedy Space Center/Cape Canaveral (KSC/CC), Wallops (W), and Vandenburg Airforce Base (V/VS) were selected, if they took place between January 1st, 2016, and December 31st, 2017. Once the payloads for each launch were identified based on their COSPAR designation, the mass of each payload, and the inclination and semi-major axis of their orbit was collected. The semi major axis was used to calculate the c3 value for each payload. Launches where payload data was missing were removed from the data pool.

For launches with a full data set, a total payload mass, inclination, and c3 value was calculated. The c3 value for the launch was taken to be the a weighted average of the c3's for each payload, weighted by mass. The inclination launch was taken to be the average inclination for each payload item.

Next, launches were categorized based on launch vehicle. Then, for each launch, a spare payload was calculated. This calculation was performed conservatively, by defining spare payload as the difference between a given launch's payload, and the maximum payload carried by the same launch vehicle, on a launch with an equal or higher c3. This definition means that many flights have zero spare payload, but ensures that the spare payload estimate is based off of the payload capabilities that have been demonstrated by each launch vehicle.

For recent years (2016, 2017), many launches took place on launch vehicle variants that only had one flight. Many launches also took place on launch vehicles that had few enough flights that no spare payload could be calculated. For 2016-2017, Only the Falcon 9 and Atlas V 401 had enough launches to define spare payload. Therefore, only these launch vehicles were used to predict future spare payload capacity.

To predict future launch capacity, launches were randomly generated based on the historical launch data. The distribution of launch vehicles in 2016 and 2017 was used to randomly select a launch vehicle from the pool of launch vehicles for which spare payload was calculated. Once a launch was chosen, a launch profile was randomly selected from the launches

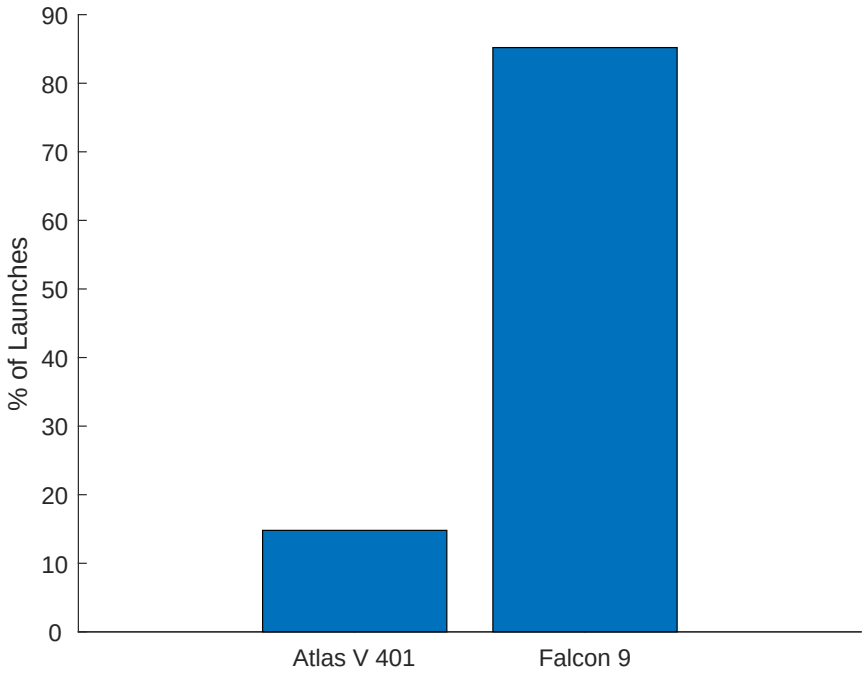

Figure 2: A histogram of of randomly generated future launches consistent with historical launch data. The x axis is the type of launch vehicle, and the blue bars indicate the percentage of future launches that will use that vehicle.

for that vehicle from 2016 to 2017. The payload, spare payload, launch site, inclination, and c3 for that launch were taken to be the values for the randomly generated launch.

Figure 3 shows 1000 randomly generated launches describing the projected distribution of future launches. The results from this analysis were that the majority of launches have little to no spare payload, and are launched on geosynchronous transfer orbits (GTO), which have little to no inclination. Fewer launches are to low Earth orbit, or are launched to a high inclination or polar orbit, and 43% of launches have more than 500 kg of spare payload.

To determine the number of modules that could be launched, random launches were generated for 7 years, with each year containing 34 launches (the total number of relevant US launches in 2018, and therefore a conservative estimate that doesn't project any growth in the orbital launch market).

These values for spare payloads were then run through Equations 1 and 2 to determine the maximum number of modules that could be launched. This calculation relied on the assumption that ESPA rings were being used to mount the modules to the rocket. The maximum number of modules able to be attached to a ring (n_{max}), and the mass of the ESPA ring m_{ESPA} were drawn from manufacturer data[4]. m_s is the mass of a single module (150 kg), m_{FL} is the mass of a fully loaded ESPA ring, and P_m is the spare payload mass.

$$m_{FL}(m_s, m_{ESPA}, n_{\max}) = m_s * n_{\max} + m_{ESPA} \tag{1}$$

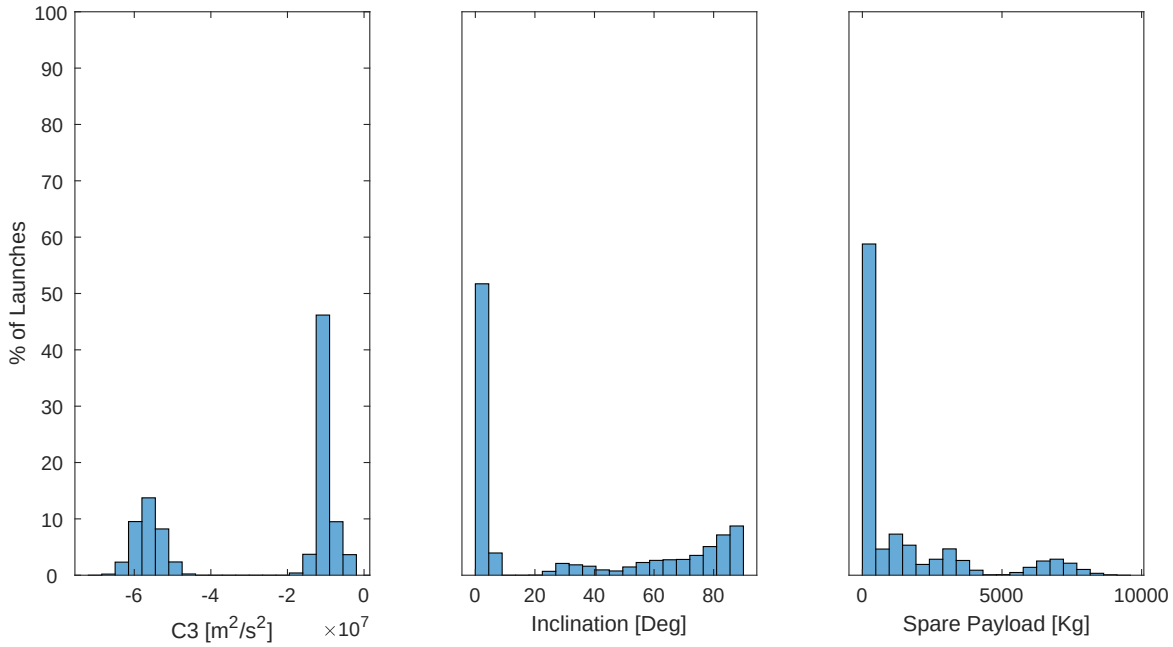

Figure 3: Histograms of randomly generated launch attributes. The figure on the left is a histogram of launch C3, the center figure is a histogram of launch inclination, and the figure on the right is a histogram of spare payload capacity.

$$N(m_s, m_{ESPA}, P_m) = n_{\max} * \left\lfloor \frac{P_m}{m_{FL}} \right\rfloor + \lfloor P_m \% m_{FL} / m_s \rfloor * m_s + m_{ESPA}. \tag{2}$$

This calculation determined that it would be possible to launch 1450 modules over a 7 year period, if current launch trends continue. This indicates that the current rate of launches would be sufficient to launch all 840 modules as payloads of opportunity in less than 7 years, with no dedicated launches required.

3 Rendezvous

3.1 Dynamic Model

The trajectory design for rendezvous near the L2 point is framed in the Circular Three Body problem, which yields equations of motion (Equation 5) for state variables (Equation 4) [5]. This formulation is based off of an approximation in which the Earth and the Sun are on circular orbits about their barycenter. The equations of motion are derived in a reference frame that rotates to keep the x-axis parallel with the line between the Earth and the Sun. The y-axis is parallel with the Earth's velocity, and the z-axis is consistent with the right hand rule (Figure 4).

The effective potential for an object interacting with the gravity of these two objects, in the rotating frame, is expressed in Equation 3. For additional information on this formulation,

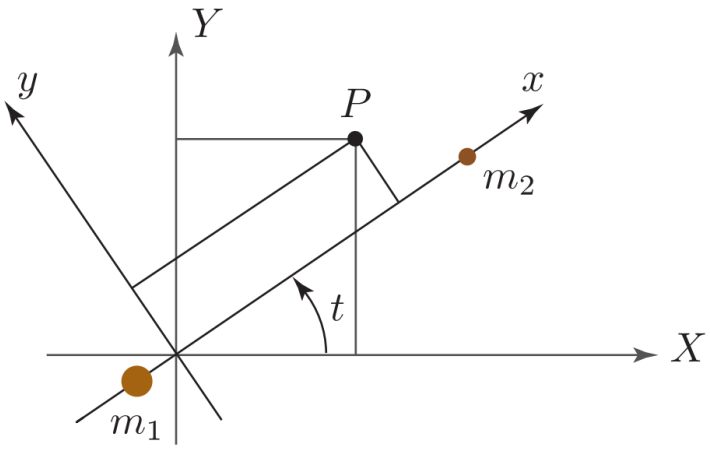

Figure 4: This figure shows the definition of the rotating frame $\mathscr{R}$ in the Circular Three Body Problem. The X and Y axis are in an inertial frame $\mathscr{I}$. x and y are in the rotating frame. $m1$ is the more massive of the two objects (the Sun), m2 is the less massive of the two objects (the Earth), and P is a particle of interest (a module).[5].

please refer to *Dynamical Systems, the Three-Body Problem and Space Mission Design* [5].

$$\Omega(x,y,z) = \frac{1}{2}(x^2+y^2) + \frac{1-\mu}{r_1} + \frac{\mu}{r_2}. \tag{3}$$

$$\mathbf{x} = [\,\mathbf{r}\;\;\mathbf{v}\,]^T = [\,x\;\;y\;\;z\;\;\dot{x}\;\;\dot{y}\;\;\dot{z}\,]^T. \tag{4}$$

$$\dot{\mathbf{x}} = \mathbf{f}(t,\mathbf{x}) = \begin{bmatrix}\dot{\mathbf{r}}\\ \dot{\mathbf{v}}\end{bmatrix} = \begin{bmatrix} \dot{x} \\ \dot{y} \\ \dot{z} \\ 2\dot{y} + \frac{\partial \Omega}{\partial x} \\ -2\dot{x} + \frac{\partial \Omega}{\partial y} \\ \frac{\partial \Omega}{\partial z} \end{bmatrix} \tag{5}$$

3.1.1 Solar Sail Model

Each module is equipped with a square solar sail, with a side length of 35 meters. These sails are assumed to perform ideally, with the sail modeled as a perfect reflector [6, 7]. The acceleration due to a sail modeled in this way is given by Equation 6.

$$\mathbf{a}_S = \beta \frac{1-\mu}{r_1^2}(\hat{\mathbf{r}}_1 \cdot \hat{\mathbf{n}})^2 \hat{\mathbf{n}} \tag{6}$$

Here, $\hat{\mathbf{r}}_1$ is the position vector from the Sun to the spacecraft and $\hat{\mathbf{n}}$ is a unit vector normal

to the solar sail. The components of $\hat{\mathbf{n}}$ can be expressed in a sail frame $\mathscr{S}$, as described below:

$$\hat{\mathbf{s}}_1 = \hat{\mathbf{r}}_1 \tag{7}$$

$$\hat{\mathbf{s}}_2 = \frac{\hat{\mathbf{z}} \times \hat{\mathbf{s}}_1}{|\hat{\mathbf{z}} \times \hat{\mathbf{s}}_1|} \tag{8}$$

$$\hat{\mathbf{s}}_3 = \hat{\mathbf{s}}_1 \times \hat{\mathbf{s}}_2 \tag{9}$$

The $\mathscr{S}$ frame is convenient, as it it simplifies the expression of $\hat{\mathbf{n}}$ in terms of spherical clock and pitch angles, δ and α.

$$\hat{\mathbf{n}} = \begin{bmatrix} \cos(\alpha) \\ \sin(\alpha)\cos(\delta) \\ \sin(\alpha)\sin(\delta) \end{bmatrix} \tag{10}$$

These angles allow the force from the solar sail to be re-defined as Equation 11.

$$\mathbf{a}_S = \beta \frac{1-\mu}{r_1^2} \cos^2(\alpha) \hat{\mathbf{n}} \tag{11}$$

β is a non-dimensional number that represents sail performance, and represents the ratio between maximum sail force and the force of gravity. It is defined in Equation 12. σ is the areal loading factor for the spacecraft (Equation 14), and $\sigma*$ is a constant (Equation 13). $L_\odot$ is the solar luminosity at 1 Au, m_T is the total mass of a module, A_s is the area of the sail, m_p is the mass of the module without the sail, and m_s is the mass of the sail.

$$\beta = \frac{\sigma^*}{\sigma} \tag{12}$$

where σ is the total areal loading factor of the spacecraft and σ^* is a constant equal to

$$\sigma^* = \frac{L_\odot}{2\pi G M_\odot} \tag{13}$$

$$\sigma = \frac{m_T}{A_s} = \frac{m_p + m_s}{A_s} = \frac{m_p}{A_s} + \sigma_s \tag{14}$$

The force from the solar sail can be used to augment the unforced equations of motion, (Equation 5, to generate new equations of motion with a control input ($\mathbf{u}$). The solar sail equations of motion can be seen in Equation 15. Here, the control input consists of the clock and pitch angles: $\mathbf{u} = [\delta, \alpha]^T$

$$\dot{\mathbf{x}} = \mathbf{f}(t, \mathbf{x}, \mathbf{u}) = \begin{bmatrix} \dot{x} \\ \dot{y} \\ \dot{z} \\ 2\dot{y} + \frac{\partial \Omega}{\partial x} + \mathbf{a}_S \cdot \hat{\mathbf{x}} \\ -2\dot{x} + \frac{\partial \Omega}{\partial y} + \mathbf{a}_S \cdot \hat{\mathbf{y}} \\ \frac{\partial \Omega}{\partial z} + \mathbf{a}_S \cdot \hat{\mathbf{z}} \end{bmatrix} \tag{15}$$

3.1.2 Optimal Control Theory

Optimal Control theory can be used to optimize trajectories, [8, 9, 10], where a cost function (J) is minimized in the interval $[t_0, t_F]$ (Equation 16).

$$J = \phi(\mathbf{x}(t_F)) + \int_{t_0}^{t_F} L(t, \mathbf{x}, \mathbf{u})\, dt \tag{16}$$

This cost function depends on both the chosen states $\mathbf{x}$ and the control input $\mathbf{u}$. Optimizing the trajectory and the control input are subject to the equations of motion , and the initial conditions. For the optimization discussed here, no terminal cost function will be used.

A Hamiltonian will be used to solve this optimization problem, and it is defined in Equation 17

$$H(t, \mathbf{x}, \mathbf{u}, \lambda) = L(t, \mathbf{x}, \mathbf{u}) + \lambda^T \mathbf{f}(t, \mathbf{x}, \mathbf{u}). \tag{17}$$

The Hamiltonian has the addition of Lagrange multipliers, which vary with time just as the state variables do. Therefore, Lagrangle multipliers are added to the state vector, with Equations of motion set by Equation 18.

$$\dot{\lambda} = -\left(\frac{\partial H(t, \mathbf{x}, \mathbf{u}, \lambda)}{\partial \mathbf{x}} \right)^T. \tag{18}$$

The optimal control law can be found by solving Equation 19, which follows Pontryagin's Maximum Principle.

$$\frac{\partial H(t, \mathbf{x}, \mathbf{u}, \lambda)}{\partial \mathbf{u}} = \mathbf{0}. \tag{19}$$

3.1.3 Optimal Control with an Unconstrained Thruster

To get an initial estimate for a trajectory, it is often useful to model a spacecraft as having unconstrained thrusters, that can provide arbitrary force in an arbitrary direction [9]. Here, the control input is the thrust vector (Equation 20).

$$\mathbf{u} = u_1 \hat{\mathbf{x}} + u_2 \hat{\mathbf{y}} + u_3 \hat{\mathbf{z}}. \tag{20}$$

This changes the Equations of motion, which can be seen in Equation 21.

$$\dot{\mathbf{x}} = \mathbf{f}(t, \mathbf{x}, \mathbf{u}) = \begin{bmatrix} \dot{x} \\ \dot{y} \\ \dot{z} \\ 2\dot{y} + \frac{\partial \Omega}{\partial x} + u_1 \\ -2\dot{x} + \frac{\partial \Omega}{\partial y} + u_2 \\ \frac{\partial \Omega}{\partial z} + u_3 \end{bmatrix} \tag{21}$$

A trajectory can be found that minimizes control effort by using a quadratic control usage cost function (Equation 22).

$$J = \int_{t_0}^{t_F} \frac{1}{2} \mathbf{u} \cdot \mathbf{u} dt \tag{22}$$

Using optimal control theory, this leads to a new Hamiltonian (Equation 23), which, when solved for the optimal control law with Equation 19, yields the relationships seen in Equations 24-26.

$$H(t, \mathbf{x}, \mathbf{u}, \lambda) = \frac{1}{2} \mathbf{u} \cdot \mathbf{u} + \lambda^T \mathbf{f}(t, \mathbf{x}, \mathbf{u}). \tag{23}$$

$$u_1 = -\lambda_4 \tag{24}$$

$$u_2 = -\lambda_5 \tag{25}$$

$$u_3 = -\lambda_6 \tag{26}$$

This allows the control input to be integrated, with Equation 18. A boundary value problem can then be solved, with boundary conditions outlined in Equation 27. This BVP can be solved using a collocation method, where the initial and final values for λ are free parameters. This method is useful as it can quickly calculate an optimal trajectory that can be used as the initial guess for the multiple shooting method. Its main weakness is this method relies on a fixed final time.

$$\begin{pmatrix} \mathbf{x}(t_0) - \mathbf{x}_0 \\ \mathbf{x}(t_F) - \mathbf{x}_F \end{pmatrix} = \mathbf{0}. \tag{27}$$

3.2 Minimum Time to Rendezvous

Analysis of module rendezvous is motivated by the need to determine which maneuvers can be accomplished with solar sails. The first step in rendezvous analysis was identifying the phasing of modules such that a close approach would be induced. To do this, a discretized Lissajous orbit that would last 50 years was generated. This was necessary due to the pseudo-

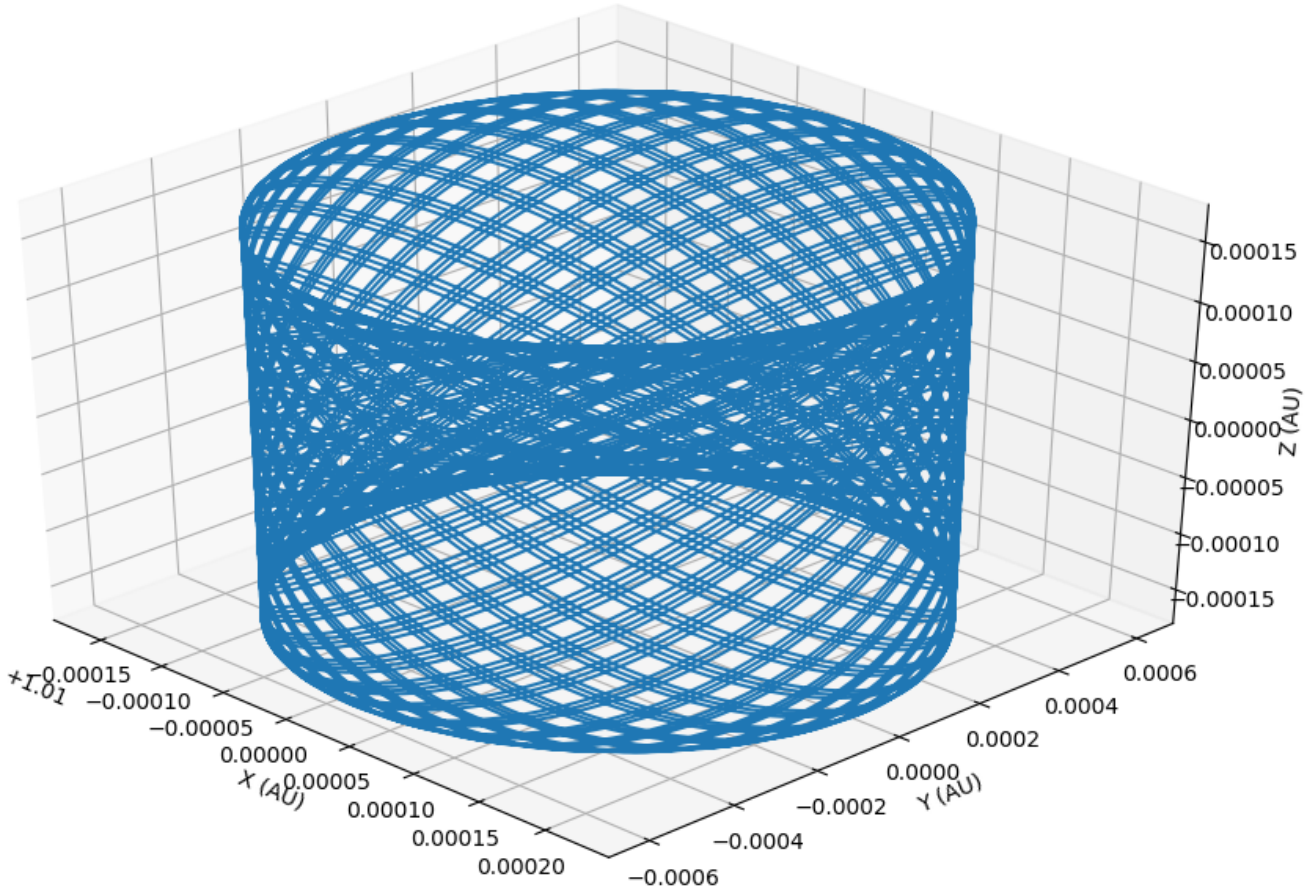

Figure 5: This figure shows the Lissajous orbit selected for the modules to be parked on during assembly. It was selected due to its ability to induce close approaches between two modules on different parts of the orbit. This figure shows 50 years of motion on the orbit.

periodic behaviour of the selected Lissajous orbit.

The Lissajous orbit selected for this part of the analysis can be seen in Figure 5

With this orbit created, the distance between each point on the orbit, and every other point, was calculated. This was done the goal of identifying locations on the orbit that had a close approach, where two modules would come within 1000 km of each other. Points within +/- 30 days of a given point on the orbit were ignored for this part of the analysis, to prevent close approaches from being identified in parts of the Lissajous orbit immediately adjacent to a given point.

This analysis showed that close approaches would be induced if modules were phased by 177.5 days on the orbit. This means that if a module is randomly placed on the Lissajous orbit, it will have a close approach with a module placed 177.5 days ahead of it on the orbit, or 177.5 days behind it. For the following rendezvous simulations, modules were placed near where close approaches were identified, to reduce the amount of the trajectory that needed to be simulated.

Once two modules were appropriately placed on the lissajous orbit, they were assigned

roles. One was arbitrarily designated as the leader, which would move passively on the Lissajous orbit, and the other was designated as the follower, which uses control to match the leader's position and velocity. The first attempt at developing rendezvous trajectories involved modeling the propulsion system as an unconstrained thruster, capable of producing arbitrary thrust in an arbitrary direction, with no change in the module's mass. Using optimal control, with a cost function minimizing control input, trajectories and control inputs were generated, with the time to rendezvous set to 1.45 days.

These trajectories and control inputs were used as the initial guess for the multiple shooting method, which was used to solve for the trajectories and control input for a module with a solar sail. Additionally, the multiple shooting method was set to minimize time to rendezvous, and used Equation 28 as the cost function to minimize. Here, t_0 is the time at close approach, and t_f is the time at rendezvous. In contrast to the unconstrained thruster optimal control solution, this method set the time at rendezvous, t_f, as a free parameter, to be updated every iteration along with the positions and velocities at each segment. Since the position and velocity of the lead satellite at rendezvous is a function of t_f, these values were updated as final time changed, requiring the terminal constraint equation to be updated every iteration. The terminal constraint can be seen in Equation 29. Here, $\mathbf{x_1}(t_f)$ and $\dot{\mathbf{x}}_\mathbf{1}(t_f)$ are the position and velocity of the lead satellite at t_f. $\mathbf{x_2}(t_f)$ and $\dot{\mathbf{x}}_\mathbf{2}(t_f)$ are the position and velocity of the follower at the final time.

$$L = \int_{t_0}^{tf} dt \tag{28}$$

$$\begin{bmatrix} \mathbf{x_1}(t_f) - \mathbf{x_2}(t_f) \\ \dot{\mathbf{x}}_\mathbf{1}(t_f) - \dot{\mathbf{x}}_\mathbf{2}(t_f) \end{bmatrix} = \mathbf{0} \tag{29}$$

Rendezvous were generated throughout the Lissajous trajectory, to ensure the solar sail was capable of producing a rendezvous trajectory regardless of the direction of the initial and final velocity, as this varies greatly depending on the location on the Lissajous orbit.

100 rendezvous were simulated; a histogram of the time to rendezvous for these simulations can be seen in Figure 6. This indicates that modules can rendezvous regardless of their position on the orbit. A peak is identified for final times between 1.5 days and 2 days. The multiple shooting algorithm is not deterministic; increasing the number iterations for each rendezvous increases the chances of identifying the true minimum time trajectory. However, the majority of the rendezvous events simulated have a time to rendezvous greater than the initial guess of 1.45, so it is reasonable to assume that this is close to the true minimum time to rendezvous for most of the simulated events, as no rendezvous events were found to have a time to rendezvous of less that one day.

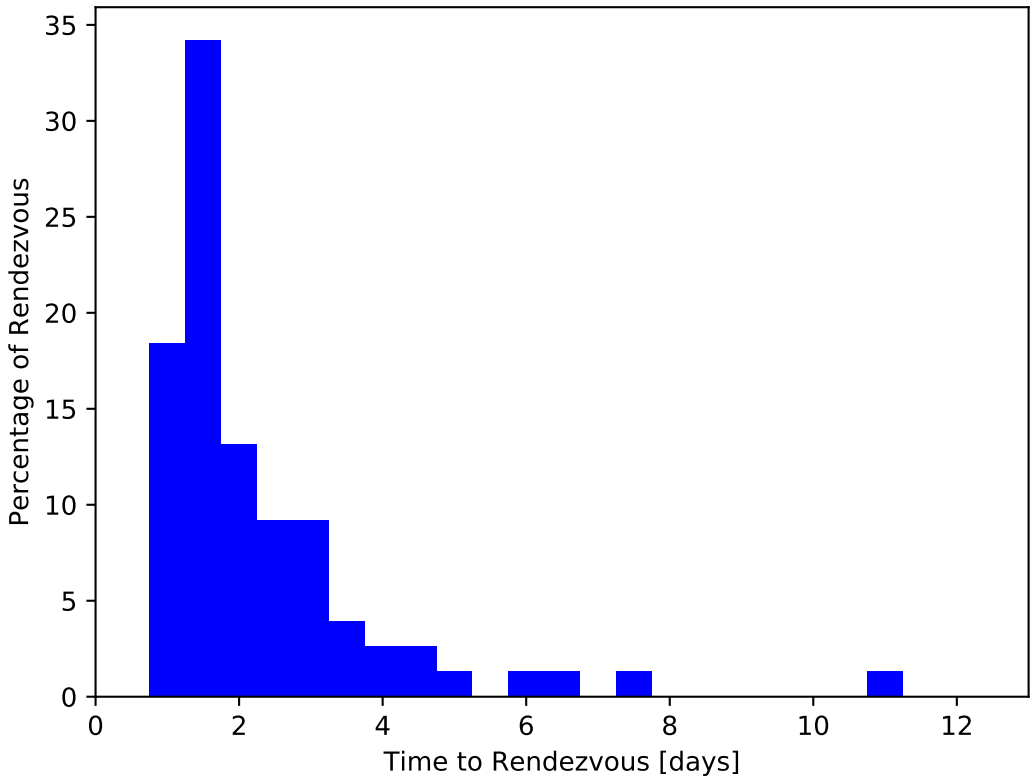

Figure 6: This figure is a histogram of the time to rendezvous for modules using a solar sail. The x axis is the time to rendezvous in days, the the blue bar represents the percentage of simulated rendezvous that took that amount of time to rendezvous.

4 Docking

4.1 Docking Pattern

Analysis of the docking procedure is required how larger groups of modules should rendezvous. The conops for this mission call for the assembly of clusters of modules, which will then rendezvous with one another for the final assembly of the primary mirror.

The first step in assessing docking is to identify how many modules should be in a cluster before it rendezvous for final assembly. It is desirable to have a low number of "precision docking events", where a module needs to navigate to a specific location on a cluster. However, it is necessary for some number of precision docking events to take place, to prevent vacant positions from being surrounded and made inaccessible, and to ensure the correct final mirror shape is created.

Additionally, it is desirable for docking events to occurred on docking sites where the vacant position is adjacent to three modules. When three modules are adjacent to a docking site, the incoming trajectory can be anywhere within a 60 degree arc, allowing for some error in the incoming module's trajectory. If four modules are adjacent to a docking site, there is

only one allowable approach direction, allowing for no error in the approach trajectory. This can be seen in Figure 7.

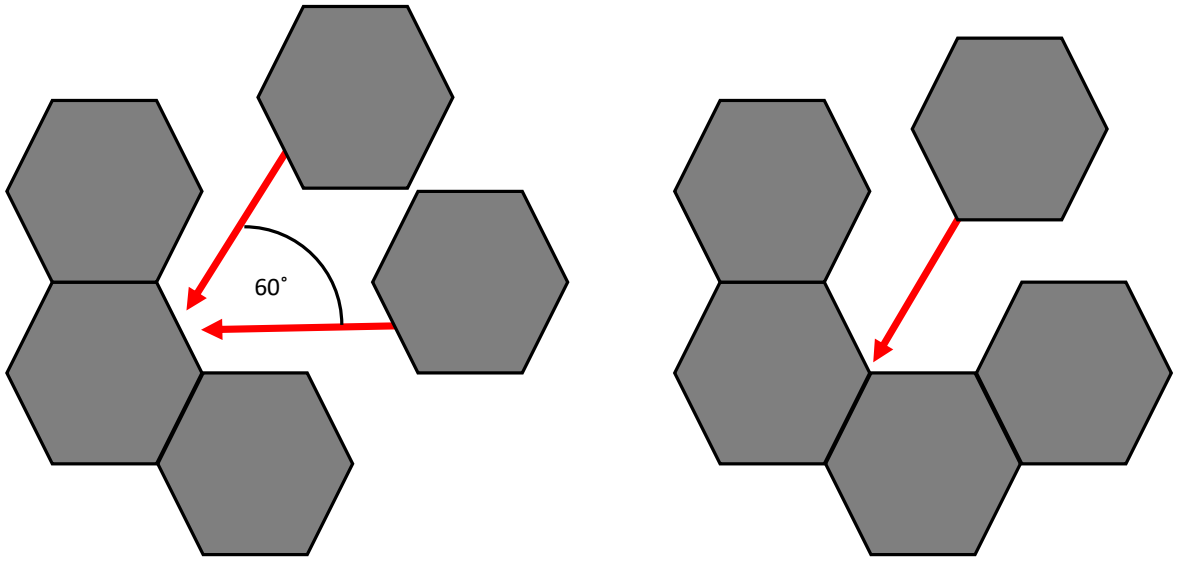

Figure 7: Top view of modules docking in two configurations. In the configuration on the left, an incoming module's trajectory may be anywhere within a 60 degree arc. However, in the configuration on the right, an incoming module only has one available trajectory.

These conditions produces a simple docking scheme, where modules are allowed to randomly add themselves to any available docking site on a cluster, unless there is a docking site that is adjacent to three modules. In that case, a precision docking maneuver must take place, where there incoming module must dock at the site with three adjacent modules.

Figure 8 shows a cluster growing using this scheme. Each frame shows the state after 5 modules have been added. This docking scheme, while simple, prevents difficult docking situations, while still allowing some modules to dock to at random sites.

4.2 Collision Mechanics

The mission concept of operations relies on modules colliding during the docking process. The modules will be equipped with embedded hook-and-loop material or hooks on the booms, so the sails/booms will stick to each other when two modules collide. Assuming modules are equipped to sense each other's orientation, the modules can use their ACS/RCS system to ensure that the booms of the solar sail are what collides first. Additionally, it will be assumed that the modules ACS/RCS system is strong enough to keep the modules in the same orientation, cancelling out any external moments from the booms during the collision.

This simplifies the problem to modeling the vibration that occurs when two cantilevered beams collide. The problem has the additional constraint that after the collision, the overlapping portions of the beams have the same position. It is assumed that the overlapping sections apply a distributed load to one another.

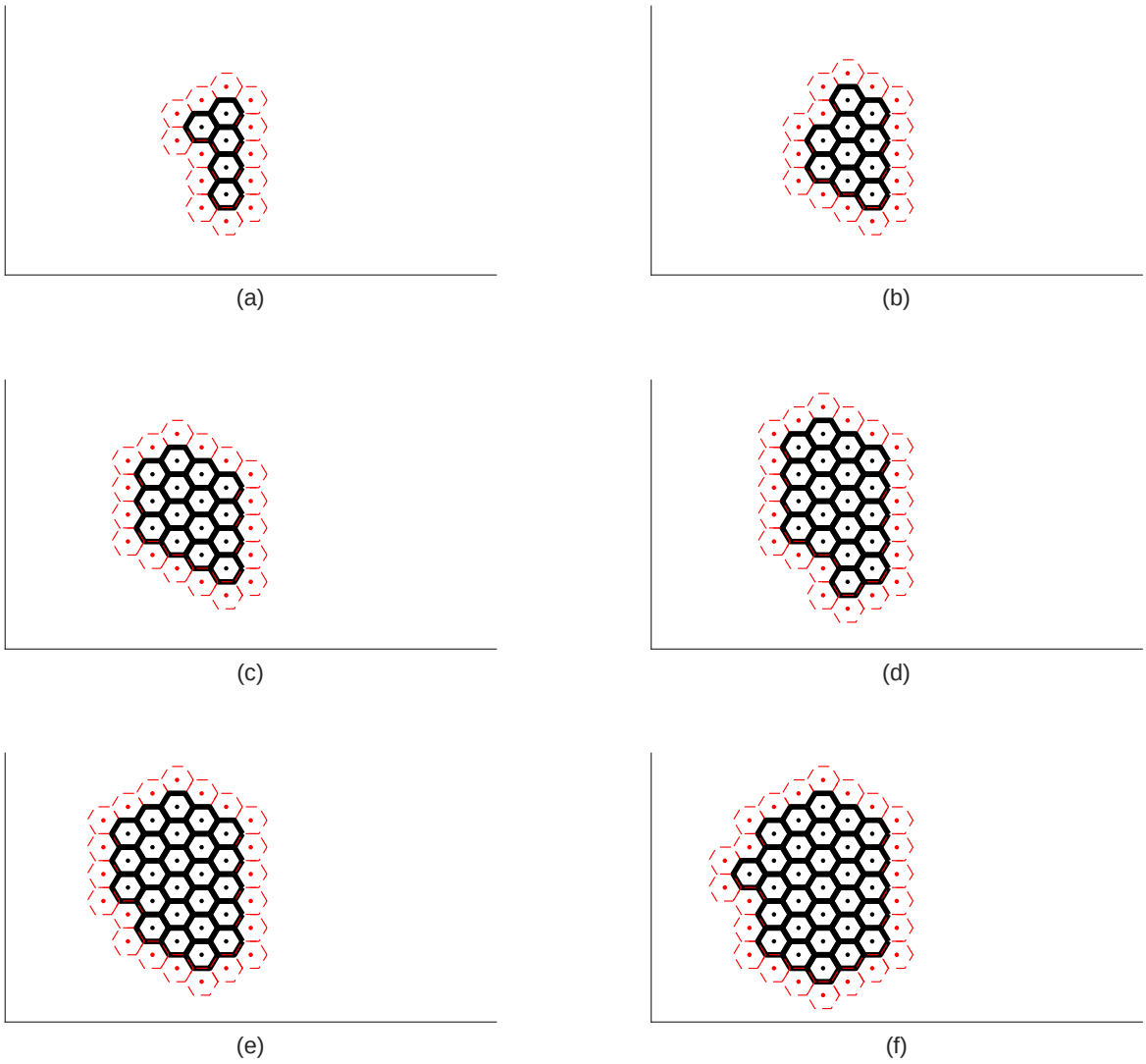

Figure 8: Top views of growing clusters of modules. Frame (a) shows the cluster after the first five modules have docked, and frames (b) through (f) show the state sequentially, with five modules docking in between each frame. The black hexagons represent docked modules, and the red dashed hexagons represent the available docking sites.

The equation for deflection of a cantilevered beam can be generalized as Equation 30, where E is the Young's Modulus of the beam, I is the area moment of inertia, δ is the deflection at distance y from the cantilever, F is the sum of the forces at the cantilever, and M is the resulting moment at the cantilever.

$$EI\delta(y) = \frac{1}{6}Fy^3 + .5My^2 \tag{30}$$

With the origin set at one of the modules during the collision, a new set of deflection equations is produced, to find the deflection in beam 1 (δ_1) or beam 2 (δ_2), where y_{sep} is the total distance between the modules.

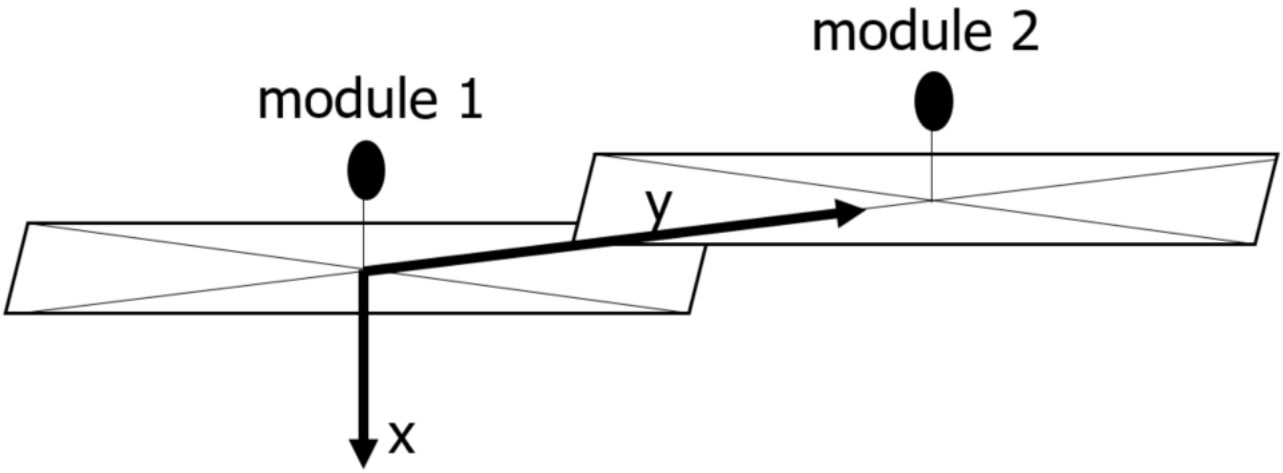

Figure 9: This shows the coordinate system used during the collision. The origin is set at the first module, and both modules move at fixed y positions, with only their x position varying during the collision.

$$EI\delta_1(y) = \frac{1}{6}Fy^3 + .5My^2 \tag{31}$$

$$EI\delta_2(y) = \frac{1}{6}F(y_{sep} - y)^3 + .5M(y_{sep} - y)^2 \tag{32}$$

These beams will have the same deflection when $y = y_{sep} - y$, which occurs when $y = y_{sep}/2$. Defining the y-axis as pointing between the modules at the moment of collision, and the x-axis as the direction of the module's motion (Figure 9). Knowing the x-separation between the modules gives the total deflection that both beams must have at the same y coordinate. Furthermore, the deflection when $y = y_{sep}/2$ must be half of the x-separation between the modules. These constraints lead to Equations 33 and 34. Now, there are at-least 2 equations, which can be used to solve for the unknown F and M. Once these quantities are solved for, the instantaneous force on each module in the x direction is known, allowing a dynamic simulation to be run of both module's motion in the x direction, with state variables $\mathbf{x} = [x_1, x_2, \dot{x_1}, \dot{x_2}]^T$.

$$\frac{EIx_{sep}}{2} = \frac{1}{6}F(y_{sep}/2)^3 + .5M(y_{sep}/2)^2 \tag{33}$$

$$x_{sep} = \delta_1(y) + \delta_2(y) \tag{34}$$

$$\mathbf{x} = [x_1, x_2, \dot{x_1}, \dot{x_2}]^T \tag{35}$$

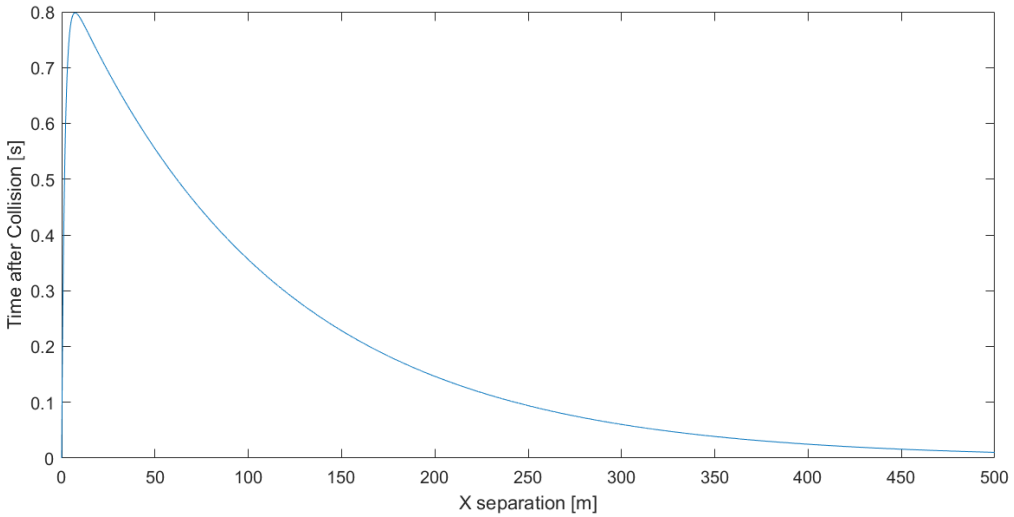

Figure 10: This figure shows x-separation between the modules during a collision. The lack of oscillations indicates the collision is over-damped.

$$\dot{\mathbf{x}} = \begin{bmatrix} \dot{x_1} \\ \dot{x_2} \\ -F + c(\dot{x_2} - \dot{x_1}) \\ F - c(\dot{x_2} - \dot{x_1}) \end{bmatrix} \tag{36}$$

While the boom design is not known, it was conservatively assumed to have a young's modulus of E = 200 GPA, an area moment of inertia of $I = 1e-8m^4$, and a density of $\rho = 1e4kgm^3$. The damping ratio was assumed to be $\zeta = 1\%$, which is another conservative estimate. Equation 37 was used to find the damping coefficient for the dynamic model [11].

$$c = (\zeta)(2)\sqrt{(}\left(\frac{E}{\rho}\right)) \tag{37}$$

A simulation was run with the initial conditions $\mathbf{x_0} = [0m, 0m, 0m/s, 0.5m/s]^T$. This models the second module colliding with the first at 0.5 m/s. The y-separation of the modules corresponded to 3 meters of overlap on the boom. Figure 10 shows the x-separation between modules during this simulation. With a maximum separation of 0.8 m, this simulation indicates the modules could withstand a collision at a higher speed, and still have the maximum boom deflection be less than 1/10th of their length, which is a requirement for the beam bending model used. Additionally, the collision exhibits over-damped behavior, which is limits oscillation between the two modules.

5 Conclusion

This analysis of launch, rendezvous, and docking indicates that a modular self assembling telescope, equipped with solar sails, is possible. There is sufficient spare payload to allow all modules to be launched in 7 years as payloads of opportunity. Modules are capable of rendezvous in a sufficiently short amount of time, and their booms are capable of dissipating energy and allowing for a smooth docking collision. While there are some questions remaining regarding docking procedure, this mission concept has been proven feasible with regards to launch, rendezvous, and docking.

References

[1] "Modular Active Self-Assembling Space Telescope Swarms." https://www.nasa.gov/directorates/spacetech/niac/2018_Phase_I_Phase_II/Modular_Active_Self-Assembling_Space_Telescope_Swarms/, 2018. [Online; accessed 10-May-2019].

[2] "Launch Log." http://www.planet4589.org/space/log/launch.html, 2018. [Online; accessed 18-Nov-2018].

[3] "Union of Concerned Scientists Satellite Catelog." https://www.ucsusa.org/nuclear-weapons/space-weapons/satellite-database#.W-HGuZNKg70, 2018. [Online; accessed 18-Nov-2018].

[4] MOOG, "ESPA User's Guide," tech. rep., 2018.

[5] W. S. Koon, M. W. Lo, J. E. Marsden, and S. D. Ross, *Dynamical Systems, the Three-Body Problem and Space Mission Design*. Marsden Books, 1.2 ed., 2011.

[6] C. McInnes, *Solar Sailing: Technology, Dynamics and Mission Applications*. Springer-Praxis Books, 1999.

[7] M. G. Q. A. A. M. M. Dachwald, Bernd, "Parametric model and optimal control of solar sails with optical degradation," *JGCD*, vol. 29, pp. 1170–1178, 2006.

[8] Z. C. B.-Z. F. Z. Y. Topputo, F., "Low-thrust minimum-fuel optimization in the circular restricted three-body problem," *JGCD*, vol. 38, pp. 1–9, 2015.

[9] E. Kolemen and N. Kasdin, "Optimization of an occulter-based extrasolar-planet-imaging mission," *JGCD*, vol. 35, pp. 172–185, 2012.

[10] C. B. A. Englander, Jacob A., "Automated solution of the low-thrust interplanetary trajectory problem," *JGCD*, vol. 40, pp. 15–27, 2016.

[11] "Cantilever Beam Static and Dynamic Response Comparison with Mid-Point Bending for Thin MDF Composite Panels." https://www.fpl.fs.fed.us/documnts/pdf2013/fpl_2013_hunt002.pdf, 2013. [Online; accessed 10-May-2019].